COMPDYN 2015
5th ECCOMAS Thematic Conference on
Computational Methods in Structural Dynamics and Earthquake Engineering
M. Papadrakakis, V. Papadopoulos, V. Plevris (eds.)
Crete Island, Greece, 25–27 May 2015

MACRO-MODEL CALIBRATION OF A STRONG CLAY MASONRY INFILL TO IN-PLANE CYCLIC TESTS

Milad A. Oliaee[1], Paolo Morandi[2], and Guido Magenes[2]

[1] ROSE School, IUSS
EUCENTRE, Pavia, Italy
e-mail: milad.oliaee@gmail.com

[2] Department of Civil Engineering and Architecture
University of Pavia, Italy

Keywords: Infills, Seismic Performance, Structural Dynamics, Earthquake Engineering, Macro Model, Calibration, Nonlinear Dynamic Analysis, Nonstructural Components

Abstract. Poor performance of reinforced concrete infilled frame buildings observed in recent post-earthquake reconnaissance may underline a deficiency in our knowledge on the seismic behavior of RC buildings with masonry infills. Past experiments have lacked tests on strong infills recently introduced in modern construction practices in Europe. As the strong typology significantly influences global building behavior, a comprehensive appraisal of the seismic performance for both full and open infill panels will improve our assessment of building performance. A recent experimental campaign on single-story RC frames infilled with a strong masonry typology has been carried out to evaluate and identify drift indices at the damage and ultimate limit state. Calibration of a macro model to the data has improved the accuracy of a macro model for nonlinear dynamic analysis of infilled RC frame buildings. Specific focus on the hysteretic properties of the frame and infill elements in the numerical model has brought significant improvement in accuracy. The need to model local effects has been circumvented by special interpretation of the experimental data. In particular, the infill's effect on the global behavior of the infilled frame subassembly has been extracted by taking comparing the hysteresis of the infilled frame and the bare frame at matching target drifts. The macro model's hysteresis rules are specifically intended for infill struts and have been adjusted for the strong infill typology. A smooth hysteresis closely mimics the tangent stiffness of the reloading and unloading branches to better match energy dissipation, strength, and stiffness. The strength envelope has been modified to account for a post-peak strength plateau exhibited by the strong infill. The results from the parametric optimization may be implemented in nonlinear dynamic analyses with adjustment to existing empirical equations that estimate the strut properties per the masonry characterization.

1 INTRODUCTION

Macro models capture the global response of masonry infills by reducing the number and complexity of finite elements required to obtain accurate numerical results, particularly for nonlinear dynamic modeling. The infill strut calibration serves as an opportunity to best match the experiment subassembly and extrapolate the results to other geometries in a real building model. Because the strong masonry infill overwhelmingly participates in the building response, special attention has been given to strength properties and hysteretic parameters to capture the net effect of the infill on the global seismic performance. For that purpose, the macro model has been optimized to determine the characteristics of the strong infill to be included in the performance-based design and assessment of buildings.

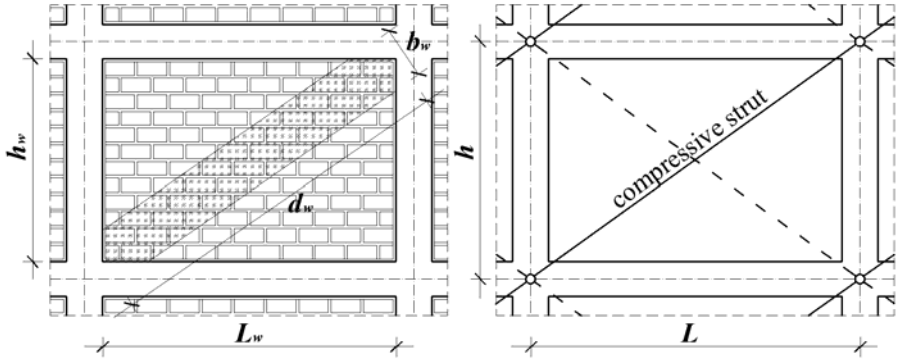

Figure 1: Equivalent diagonal single-strut model.

In general, the strength, energy dissipation and stiffness of the response represent important criteria for making modeling decisions. Due to the complexity of the hysteresis rules, the parameters cannot be independently calibrated, and the resulting optimization problem is rendered multivariate and nonlinear. A preliminary trial and error approach was unsatisfactory as the results failed to meet all the objectives of the calibration. Instead numerous combinations of the parameters are evaluated to obtain the best solution by locating the global minimum for an array of error surfaces. That is, the combination of relative error per specific strength, energy dissipation and stiffness criteria.

To reduce the size of the problem, the initial set-up procedure helps to eliminate all but three parameters from the optimization process. During the process, each error criterion is given equal weight. The best combination of parameters with the least error is chosen as the final solution. The error criteria focus on the post-peak region of the cyclic tests where the strong infill typology has demonstrated significant displacement capacity in recent tests [1].

1.1 Experimental Campaign

The strong masonry infill typology considered here represents an upper bound of the possible strength & stiffness properties a masonry infill can exhibit. The typology represents a single-leaf unreinforced masonry infill of 35 cm thickness, consisting of vertically hollowed lightweight tongue and groove clay block units, having nominal dimensions of 235 x 350 x 235 mm with a nominal volumetric percentage of holes near 50%. The mortar bed-joints consist of a general purpose mortar type M5 whereas the interlocking head-joints are without mortar. The perimeter of the infill panel has been set in complete contact with the surrounding frame.

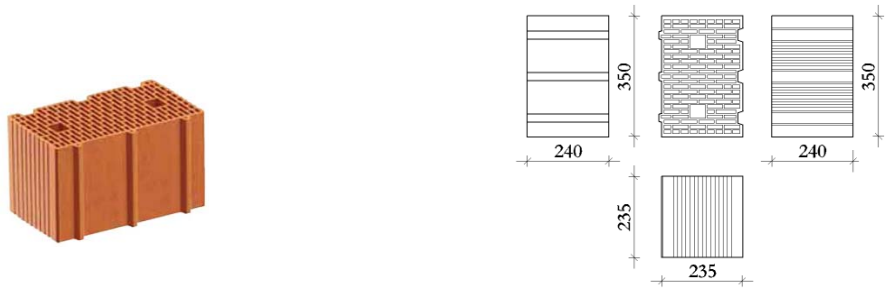

(a) (b)

Figure 2: Masonry unit (a) isometric view & (b) profile views with dimensions (mm).

A series of in-plane quasi-static cyclic tests have been carried out on a single-story, single-bay RC frames with a full infill panel, open infill panel, and no infill panel. The freames have been designed according to modern European (and Italian) code provisions.

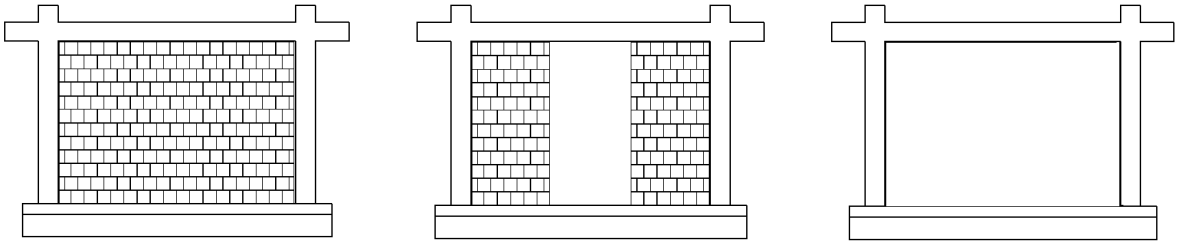

(a) (b) (c)

Figure 3: Schematic of the a) full infill panel, b) open infill panel and c) bare frame.

Prior to the cyclic tests, a detailed characterization of all material components (i.e., concrete, reinforcing steel, mortar, masonry units and masonry) has been performed [1]. An extensive numerical study on a wide range of infill typologies had hypothesized that a thicker, stronger & stiffer masonry unit could control damage at lower ground motion intensity [2]. The dry tongue and groove joints dry head joints have been known to have significant strength benefits [3].

		Reference Typology	Selected Typology
Masonry unit properties			DANESI Poroton Plan 700 TS
Nominal vertical resistance	[*MPa*]	8.0	8.0
Vertical resistance[1]	[*MPa*]	-	12.9
Horizontal resistance[1]	[*MPa*]	-	2.2
Thickness	[*mm*]	350	350
Height	[*mm*]	230 - 250	235
Percentage of holes	[%]	50 - 55	50
Minimum shell thickness	[*mm*]	4.5 - 5.0	4.8

[1]Preliminary characterization

Table 1: Strong infill masonry unit properties.

Table 1 lists the characterization of the masonry infill typology prior to full scale cyclic tests. During the cyclic tests, a single actuator applies lateral load quasi-statically along the

beam centerline (Figure 4). The end plate remains in contact with the beam cap by the fastening of steel rods to the opposing beam end. The post-tensioning force imparted to the beam varies during each half cycle of loading due to tightening and relaxation of the tendons.

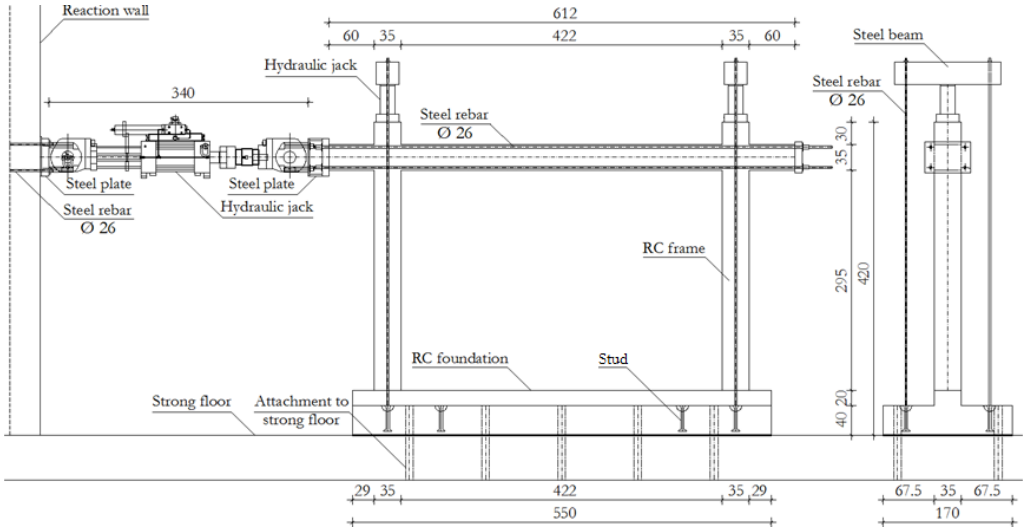

Figure 4: Front & side view of the experiment apparatus mounted on the bare frame specimen.

A comparison of the hysteresis and the average peak envelopes are shown for the fully infilled frame and infilled frame with a one-third bay length opening in Figure 5. The drift indices indicating limit states have been defined according to EC8 and NT8 [4, 5].

Taking into account the infill damage propagation observed during the test, performance levels for a single strong masonry infill with and without the opening have been defined as illustrated in Figure 5. For the infill without an opening, a 0.50% drift index has been assigned for the damage limit state and 1.75% drift index for the ultimate limit state. For the case of the infill with the opening, drift values of 0.35% and 1.0% denote the damage and ultimate limit states, respectively. In both the cases, an operational limit state, equal to 2/3 the damage drift index has been selected in accordance with seismic design provisions but not indicated on the plots.

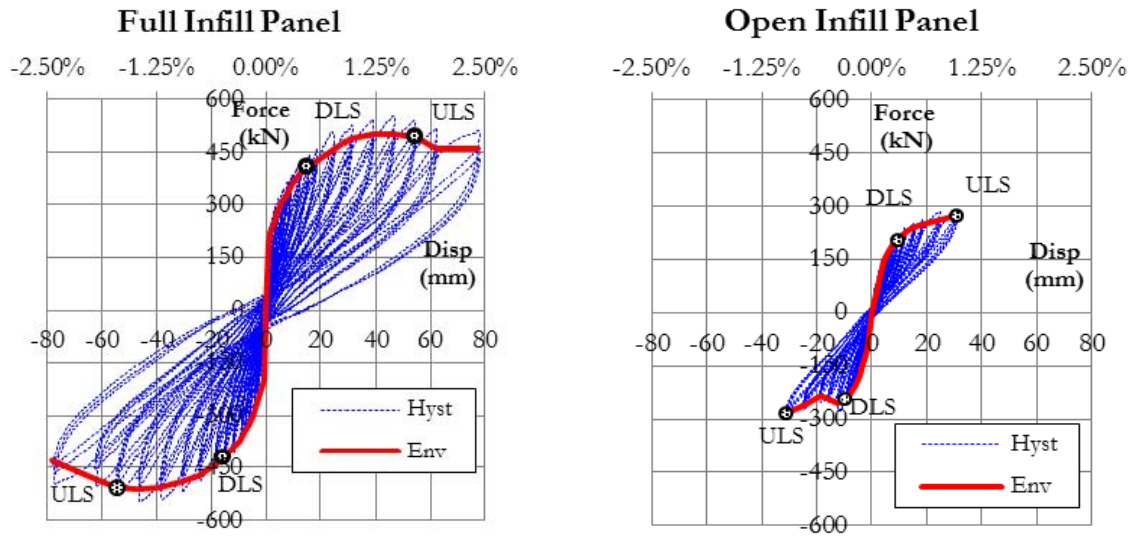

Figure 5: Hysteresis and envelope of the RC frame response with the full infill panel and open infill panel.

1.2 Interpretation of the Experimental Data

With the incentive to reduce the number of parameters during the optimization process, the infill effect's on the bare frame response is extracted by taking the difference between the response of the bare frame and the infilled frame at equal target drifts during the initial calibration procedure. The resulting hysteretic response is not just the shear contribution of the confined infill panel but also the change in the bare frame's response due to the presence of the infill panel.

The single bay specimen has the condition in which the frame members drag strut forces induced by the infill panel at low drift. Likewise for frame members without infills in adjacent bays, the effect of the strut action becomes unbalanced due to the infill bearing load onto the column faces below the joint. These forces offset the neutral axis of the concrete section and alter the plastic moment resisting capacity of the flexural hinges. For this reason, the calibration procedure for the strong infill uses the combined response of the infilled frame in relation to the bare frame response. That way the infill strut doubles to capture the shear contribution of the infill and the change in response from the bare frame as well.

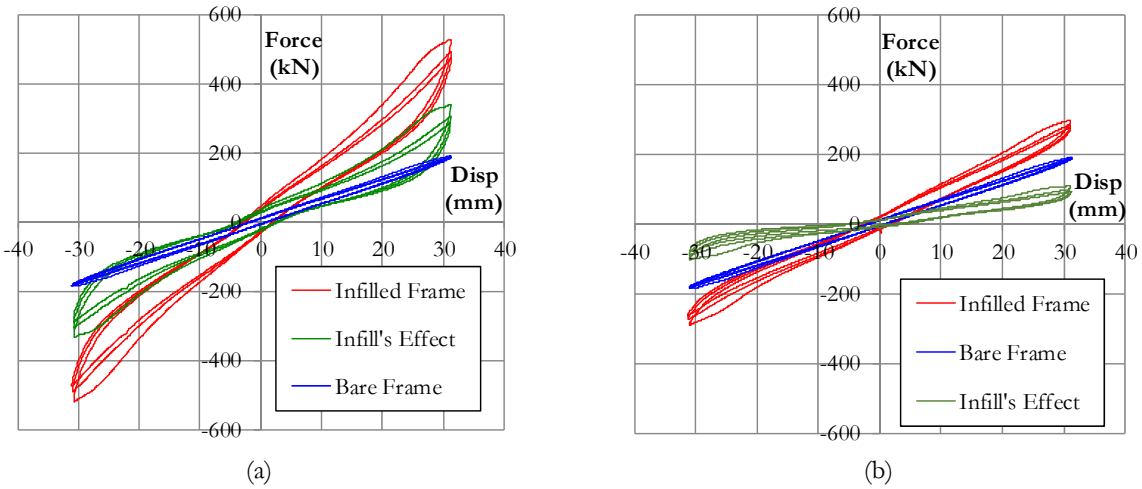

Figure 6: A portion of the hysteretic response of a) the fully infilled frame and b) infilled frame with opening.

Repeated cycles corresponding to one percent drift are shown above in Figure 6 for the two different infill configurations. The net effect of the infill is shown in green. For the fully infilled frame, the infill's effect exceeds the bare frame response and thus dominates resistance to lateral load. The infill with the opening shows less resistance than that of the bare frame.

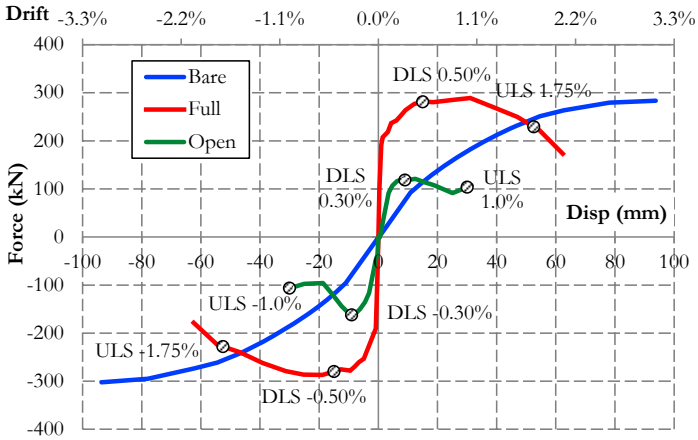

Figure 7: The envelope curves averaging the cyclic peaks of net infill's effect on story shear.

The strength and stiffness of the infill strut ultimately influence the amount of interaction between the bare frame plastic hinges and the strut action of the infill in the numerical model. The envelope of the average peaks for the full and open infill panels with respect to the bare frame are shown above in Figure 7.

1.3 Bare Frame Model Parameters

Before the infill strut parameters are chosen, the beam-column element properties are calibrated to the bare frame response. Because closely spaced stirrups provide confinement along the entire length of the column, the plastic hinge curvature ductility is left unchanged. Perhaps the most important parameters for modeling the RC frame are the axial-moment yield surface and the reduced unloading/reloading rotational stiffness of the hysteretic rules. These parameters dictate the cyclic development of shear resistance by the bare frame in combination with the infill strut.

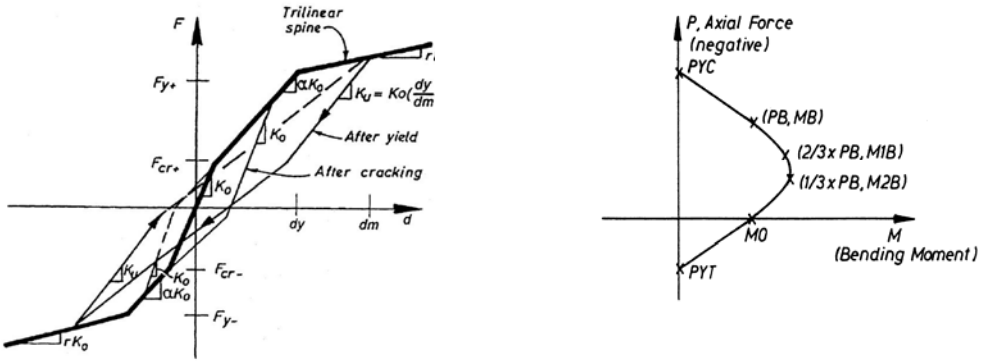

(a) (b)

Figure 8: The rotational spring hysteresis (a) and the axial force-bending moment interaction surface (b).

The beam-column elements have lumped plasticity offset from each end [6]. The inelastic rotational springs have a trilinear moment-curvature spline. The beam-column yield interaction surface for the concrete connects intermediate points via a cubic spline (see Figure 8). The smooth spline interpolation is advantageous over a straight line interpolation for condition in which the axial force varies widely. The reduced reloading stiffness factor have been set higher than the beams, such the order of hinge formation is not altered.

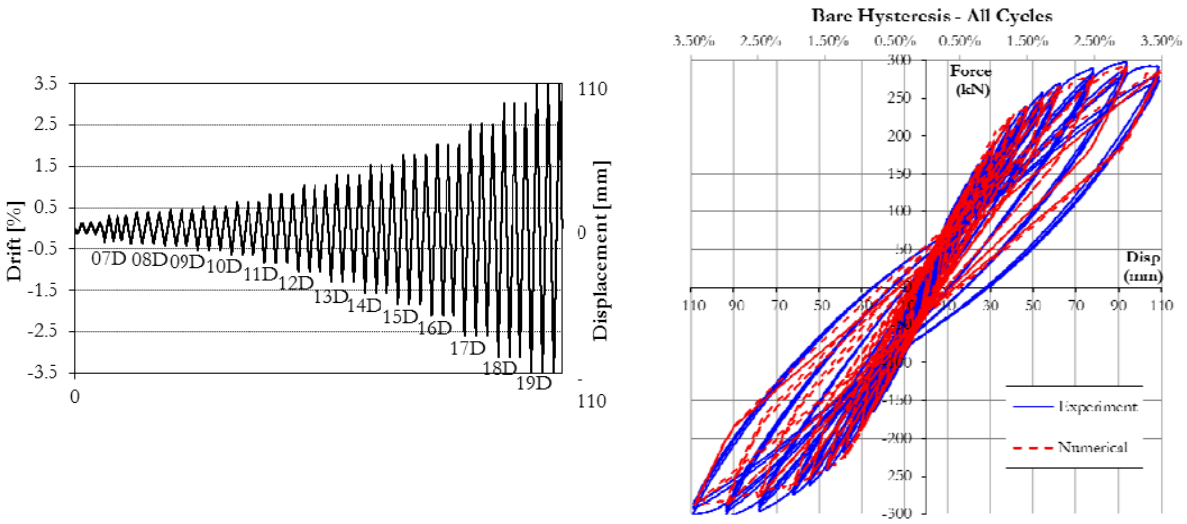

Figure 9: Displacement load history and force-displacement hysteresis of the bare frame test in comparison to the numerical model.

The bare frame model has an elastic prestressed element collinear to the beam element so when the specimen is pushed, the axial compressive force in the beam relaxes. The unloading and reloading stiffness parameters of the modified Takeda hysteresis rules influence the development of shear resistance of the frame [7].

The final values for the reloading parameter, α, are 0.17 for the beam and 0.35 for the column. The values for the unloading parameter, β, are 0.05 for the beam and 0.07 for the column. The values show a good match with the hysteresis backbone and the unloading curves at large deformations (see Figure 9). The target drift labels are shown in the displacement load history plot and they serve as a reference for the drift targets of infilled frame tests also.

1.4 Masonry Infill Model Parameters

The Decanini equations are used to estimate the strength of the infill struts depending on masonry characterization, the infill panel aspect ratio and the beam/column widths [8]. The equations adopt the strut elastic modulus $E_{w\theta}$ and stiffness parameter λ proposed by Stafford Smith [9] but also consider the mode of failures depicted in Figure 10.

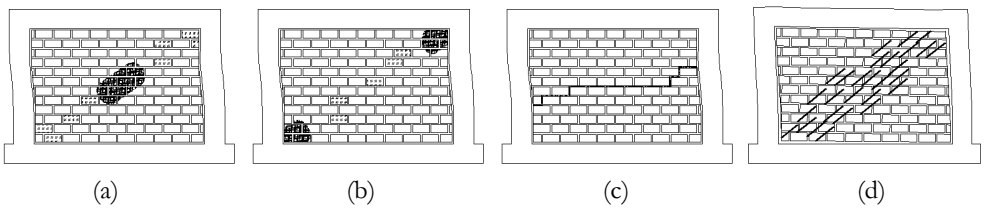

Figure 10: Diagrams for the four failure modes considered by the empirical equations: (a) Compression at the infill panel center, (b) Compression at the infill corners, (c) Sliding shear failure; (d) Diagonal tension failure.

The governing failure mode for the test subassembly is shear sliding failure, presented by Equation 1 below. The strut width for the open infill panel has been reduced according to Seah and Dawe's empirical parameter r_b that reduces the strut area based on the width of the opening [10]. r_b for an opening a third length of the bay reduces the strength to roughly half.

$$\sigma_{w_1} = \frac{(1.2 \cdot sin(\theta) + 0.45 \cdot cos(\theta)) \cdot f_{wu} + 0.3 \cdot \sigma_v}{\frac{b_w}{d_w}} \quad \text{(Shear Sliding)} \tag{1}$$

θ is the inclined angle of the strut, f_{wu} is the strength in shear sliding on a prism test, σ_v is the vertical bearing stress on the panel, b_w is the width of the strut, and d_w is the length of the diagonal. Following the model calibration to the bare frame cyclic tests, the properties of the single-strut macro model are adjusted within the user domain of Ruaumoko with the original Crisafulli hysteresis rules [11, 12]. They are tuned to best match the extracted hysteresis representing the infill shear contribution and the change in the bare frame response due to local effects. Note that during the calibration of the infilled frame, the bare frame parameters remain unchanged.

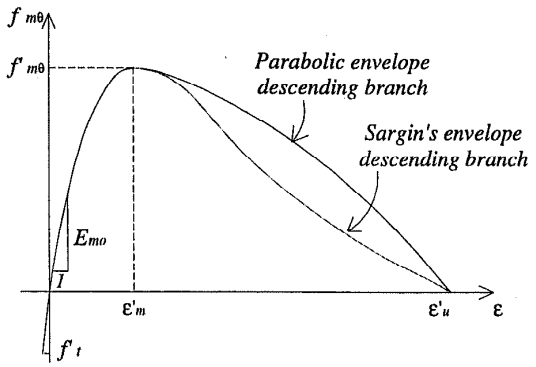

Figure 11: Comparison of the parabolic curve and Sargin's envelope.

The stress-strain constitutive model outlines the backbone that the loading and unloading paths achieve by the hysteresis rules. The original strength envelope is defined by a parabolic common for modeling cementitious materials in uniaxial compression (see Equation 2). Because the strong infill has significant post-peak strength, the alternative strength envelope, Sargin's envelope, is not ideal for the descending branch [13] but instead adopted for the ascending branch. For the descending branch, the parabolic curve is implemented but broadened a large ultimate strain such that a plastic plateau continues beyond peak resistance. For the strong masonry infill, the ultimate strain is set equal to 20 times the peak strength strain.

$$\sigma(\varepsilon) = f_m \left[1 - \left[\frac{(\varepsilon - \varepsilon_m)}{(\varepsilon_u - \varepsilon_m)} \right]^2 \right] \tag{2}$$

f_m is the maximum compressive strength, ε_m is the strain at peak strength, and ε_u is the ultimate strain at no strength. The fully infilled frame has a second plateau in the infill response beyond two percent drift and continuing to the end of the cyclic tests. The most effective way to model such behavior with the current model's platform is to decrease the strut's cross-sectional area via a piece-wise function. The starting and ending strut areas provide for the first and second strength plateaus. In between the plateuas, the intermediate softening branch is linearly interpolated. Figure 12 shows the strut area, material strength, and strut strength.

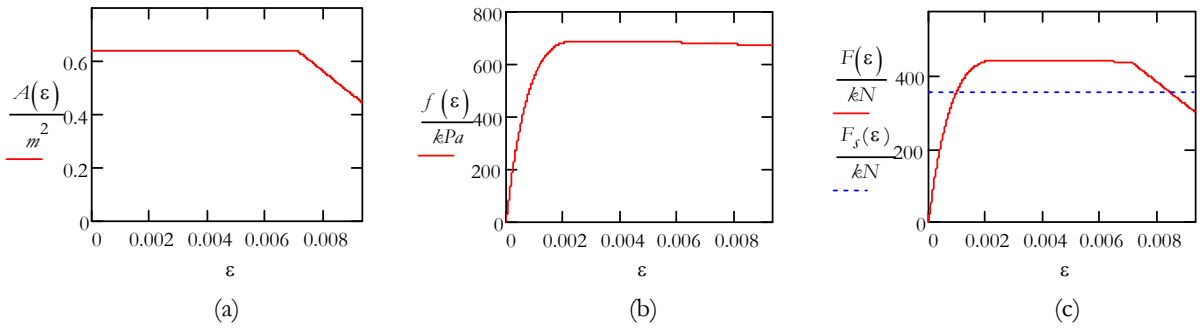

Figure 12: The strut cross-sectional area (a), axial stress (b), and axial force (c) strain relations. The dotted blue line, F_s, marks 80% force degradation.

Before the hysteresis rules are outlined, the function that provides the smooth, curved path for unloading and reloading must be presented. For every change in loading direction of the

strut, a hysteretic rule determines the starting point, ending point, initial tangent modulus, and the final tangent modulus. The values are passed to a smoothening function in the normalized strain domain to interpolate a curve between the two points with matching tangent slopes.

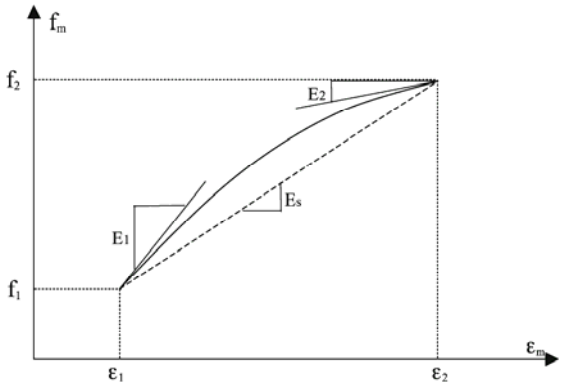

Figure 13: Conceptual plot of the interpolating curve function in the Crisafulli rules.

1.5 Hysteretic Rules

To determine the path dependent unloading and reloading points, there are four basic rules: 1) loading, 2) unloading, 3) reloading before the change point and 4) reloading after the change point. The intermediate change point separates the reloading path. It forecasts reentry to the backbone curve and transforms a convex pre-change point curve at a post-change point concave curve.

The unloading path effectively influences energy dissipation, as it provides the lower bounding edge for the hysteresis loop area. The secant modulus during unloading dictates the reduced stiffness of the strut and, in turn, elongates the transitory period of the structure. The secant unloading stiffness is used to define this effect for large displacements.

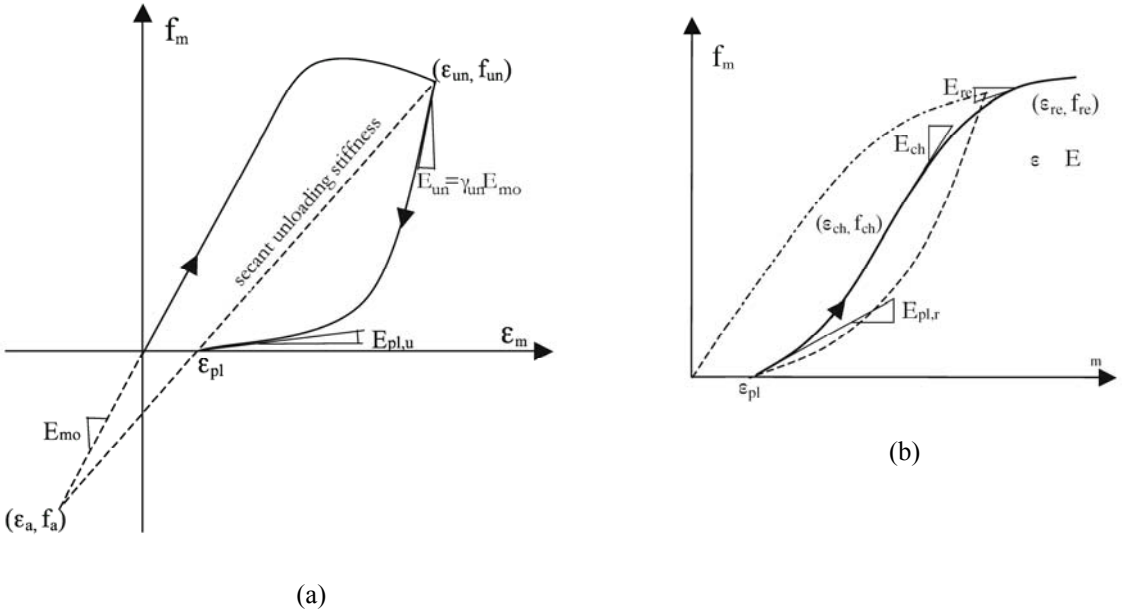

Figure 14: Conceptual plot of the unloading and reloading Crisafulli hysteretic rules.

During reloading, if α_{re} is greater than zero, the cyclic response of the infill strut falls below the virgin envelope by overshooting a reentry strain beyond the original unloading strain.

Thus α_{re} reduces the strength by calculating the strength at a larger strain on the descending branch. Thus the hysteretic loops stagger as cycles undergo increasing strain.

In addition to strength degradation at increasing strain, an empirical counter is implemented to account for in-cycle strength degradation. The repeated cycle counter is raised to a fraction of a power and reduces α_{re} in the denominator such that the cycles with repeated maximum strain have strength degradation also. In summary, the hysteretic rules capture the three basic modes of cyclic deterioration: (1) post-peak strength degradation, (2) reduced reloading stiffness, and (3) deteriorating unloading stiffness.

2 CALIBRATION PROCEDURE

Before optimization, the shape of strength envelope must be identified. The compressive strength of the strut f'_c is set to directly match the Decanini equations while the strut area A_1 is initially set to the maximum shear strength during the cyclic tests. The strain ε'_m is chosen to best represent the knee of the average envelope for the full infill panel, and the strain at peak strength for the open infill panel. The tensile strength of the strut, f_t, may be assumed to be zero. Third, for the strong infill the ultimate strain ε_u should be set to 20 times the strain ε'_m.

For the fully infilled configuration, the drop in strength to the second plateau is estimated by the average envelopes, but anchored by the initial strut area A_1 such that the drop from A_1 to A_2 at axial displacement intervals d_1 and d_2 are fixed and determined before optimization begins. For the open infilled frame, d_2 is taken as the maximum displacement during the cyclic tests. Thus the shape of the backbone remains the same during optimization.

The final parameter set before optimization is the strut elastic modulus E_{mo}. It effects the loading and unloading stiffness in the rules. Optimizing the unloading stiffness for energy dissipation in the post-peak range impedes upon the accuracy of the backbone's initial stiffness, so to compromise the elastic modulus is reduced and unloading stiffness is fine-tuned by the parameter γ_{un} during optimization (see Figure 14a).

The last remaining parameters to be determined during optimization are α_{re}, γ_{un}, and A_1. The initial strut area is included because the numerical average cyclic envelope depend on the combination of α_{re} and A_1. That is, the virgin envelope according to A_1 is reduced by α_{re}, even for the first cycle of each post-peak target drift. A strategy to identify specific attributes of the combined cyclic response has been followed to determine the best combination of parameters according to a set criteria.

2.1 Optimization Criteria

Because the model behavior varies heavily with the hysteresis path, the cyclic response renders typical optimization algorithms impractical. Instead a strategy to target specific attributes of the cyclic response has been created, and criteria help to identify the best combination of parameters. The criteria have a profound effect on the optimization process and should be defined carefully before making decisive modeling decisions.

Force To best quantify the extent to which the model of matches the peak cycles, the peak forces of the response history between the damage and ultimate state drift indices are compared.

$$Env_{err} = \frac{\sum_{i=9D}^{14D} \left(max\left(F_{exp_i}\right) - max\left(F_{num_i}\right) \right)}{\sum_{i=9D}^{14D} max\left(F_{exp_i}\right)} \tag{3}$$

Energy The sum of the normalized energy dissipation for cycles at matching target drifts of the bare and infilled frames are compared. For the fully infilled frame, there are ten possible target drifts in which the three cycles, positive and negative can be compared. For the open infilled frame, only five. The drift target indices in Equation 4 are specifically for the fully infilled frame.

$$E_{err} = \sum_{i=8D}^{17D} \left[\frac{\sum_{j=1}^{nj-1} \left[\frac{\left(F_{exp\,i,j} - F_{exp\,i,j+1}\right)}{2} \left(d_{i,j} - d_{i,j+1}\right) \right]}{\sum_{i=8D}^{17D} \left[\sum_{j=1}^{rows\left(F_{exp\,i}\right)-1} \left(d_{i,j+1}\right) \right]} - \frac{\sum_{j=1}^{nj-1} \left[\frac{\left(F_{num\,i,j} - F_{num\,i,j+1}\right)}{2} \left(d_{i,j} - d_{i,j+1}\right) \right]}{\sum_{i=8D}^{17D} \left[\sum_{j=1}^{rows\left(F_{num\,i}\right)-1} \left(d_{i,j+1}\right) \right]} \right] \tag{4}$$

Stiffness Finally, the average secant unloading stiffness for each matching cycle of the bare and infilled frames are compared. The secant loading stiffness is defined by a segment between initial unloading and the onset of reloading shown previously in Figure 14. The values of stiffness are compared to the experiment by Equation 5.

$$Stiff_{err} = \frac{\sum_{i=8D}^{17D} \left[\left(K_{exp\,i}\right) - \left(K_{num\,i}\right) \right]}{\sum_{i=8D}^{17D} max\left(K_{exp\,i}\right)} \tag{5}$$

3 RESULTS

The final surfaces for $\gamma_{un} = 7$ with the lowest global minimum error are shown in Figure 15 for the full infill and open infill configurations.

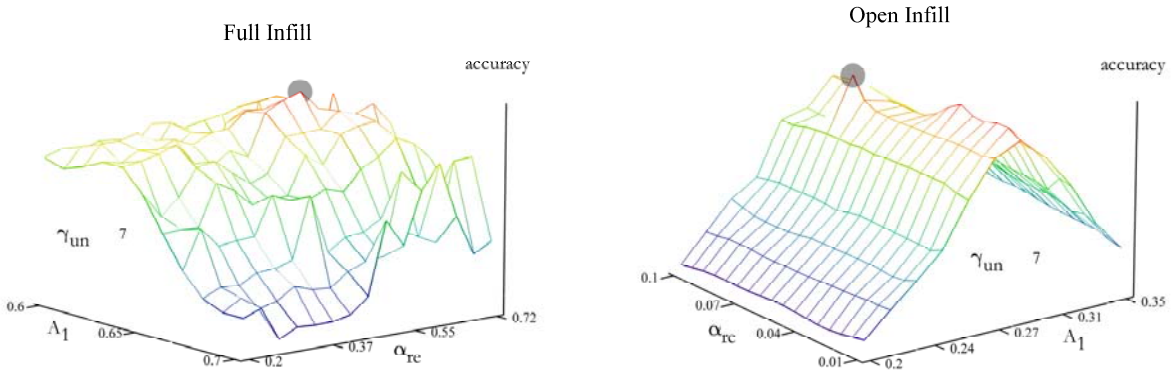

Figure 15: Final inverted error surfaces for the full infill and open infill calibrations.

Each surface represents the combined relative error based on the energy, force and stiffness criteria mentioned. Thus the point indicating the global maximum having the highest accuracy is the best solution. Accuracy is computed as the negative value of the absolute error. The final values for the fully infilled specimen and the infilled frame with opening are shown in Table 2. The results of the optimization concerning γ_{un} match for both the calibrated infill configurations. They indicate the unloading stiffness is controlled by the characteristics of the masonry and not the infill configuration.

Config	Full	Open
f'_c *(kPa)*	688	688
f_t	0	0
ε'_m	$2.10 \cdot 10^{-3}$	$1.63 \cdot 10^{-3}$
ε_u	$44.2 \cdot 10^{-3}$	$32.6 \cdot 10^{-3}$
ε_{cl}	0	0
E_{mo}	97929	97929
γ_{un}	**7**	**7**
α_{re}	**0.55**	**0.09**
A_1 *(m²)*	**0.64**	**0.294**
A_2 *(m²)*	0.4	0.221
d_1 *(mm)*	39.2	22.1
d_2 *(mm)*	52	27

Table 2: Final selection of parameters of the macro models for each configuration with values in bold found by optimization.

Also, the final value A_1 is larger than the original value of A_1 before optimization because α_{re} has reduced the cyclic response. The final parameters chosen following optimization are listed in Table 2 below. For the full infill panel, the optimized strut width complements the "one-third" rule originally proposed by Holmes in 1961 [14].

3.1 Post-Peak Envelope

The numerical and experiment envelopes match well for the fully infilled frame. Figure 16 shows the first cycle and the average peaks for the three cycles. The numerical model slightly overestimates the initial peak strength and underestimates the plateau in the post-peak region. However, the difference is relatively small and the shape of the softening branch is preserved with the exception of the first push cycle, in which there is a small drop in the strength beyond the ultimate limit state. As predicted, the numerical model underestimates the initial stiffness, analogous to the cracked stiffness in the beam-column elements.

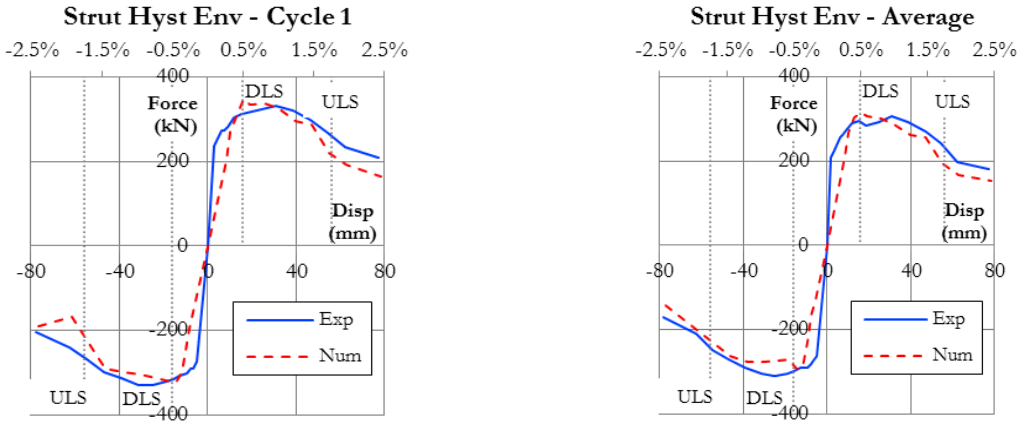

Figure 16: Envelopes of the first cycle and average of the cyclic tests for the full infill configuration.

Matching the envelope for the open infill configuration has been more challenging given the asymmetric response and the short range of experimental data viable for optimization. As seen in Figure 17, a good match has been found for the first cycle, however, the comparison to the experiment average cycles reveals a reduction in strength not captured well by the numerical model for the pull cycles. Although optimization is implemented for the push cycles

only, the pull cycles also agree with the experimental results. This result is coincidental and perhaps explained by the effect of the shape of the hysteretic loops on the energy criteria.

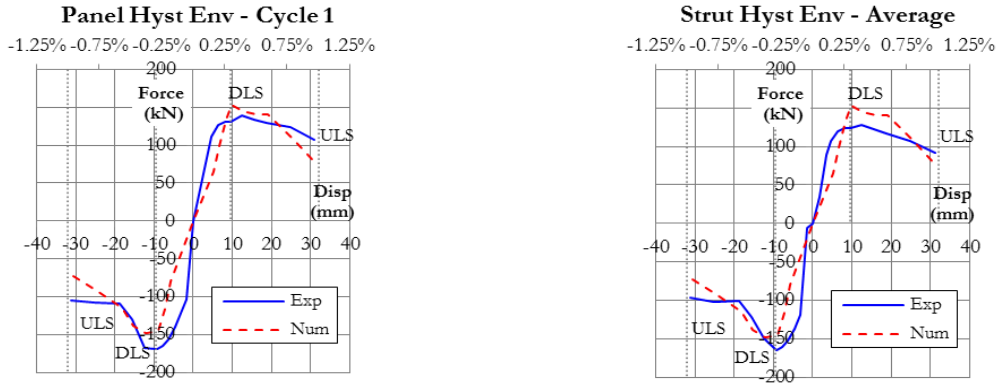

Figure 17: First cycle and average envelope comparison for the open infill configuration.

3.2 In-Cycle Effects at Repeated Drift

An interesting prospect arises when investigating the change in the hysteretic loops across sequential cycles at repetitive matching target drifts. For the fully infilled frame, the approach to the backbone curve changes from a rounded to pointed edge, which would indicate material degradation within the panel occurs only at incremental target drifts. For the cycles within a single target drift, the width of the loops decrease steadily in succession both in the experiment and in the numerical model. Also, by inferring that the unloading stiffness remains unchanged, most of the energy dissipation capacity loss arises from reloading branch cutting into the original loop profile. Because the peak force recedes with every repetition, the length of the loop also decreases, further impacting the net energy dissipation.

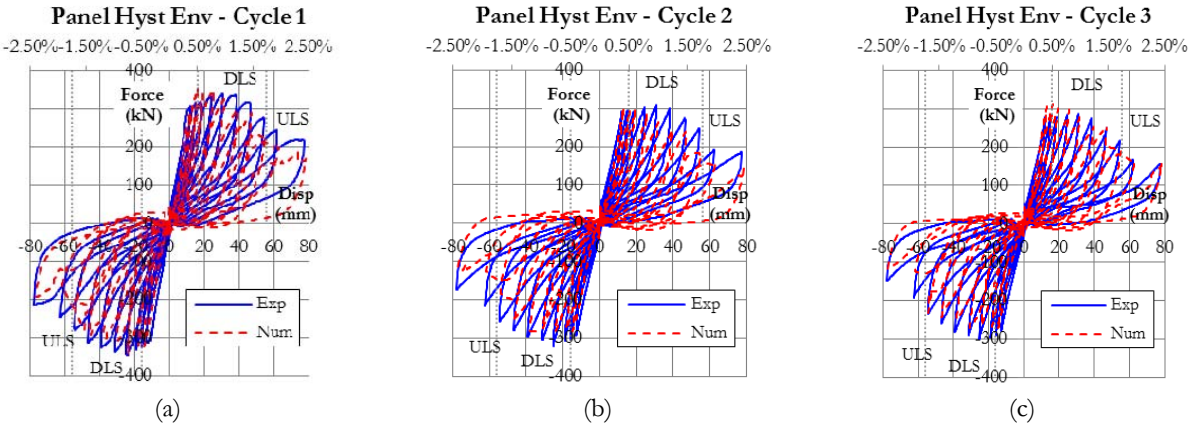

Figure 18: Effect of repeated cycles on the shape of the hysteresis for the full infill configuration.

For the open infill, the bare frame energy dissipation dominates the response following the first cycle, visible by the extreme thinning of hysteresis loops in Figure 19 below for the second and third cycle. The thickness of the loops also thin, denoting a decrease in energy dissipating capacity. There is no criteria set indicating the shape of the loops, but rather only the total area, or the net energy dissipation per cycle.

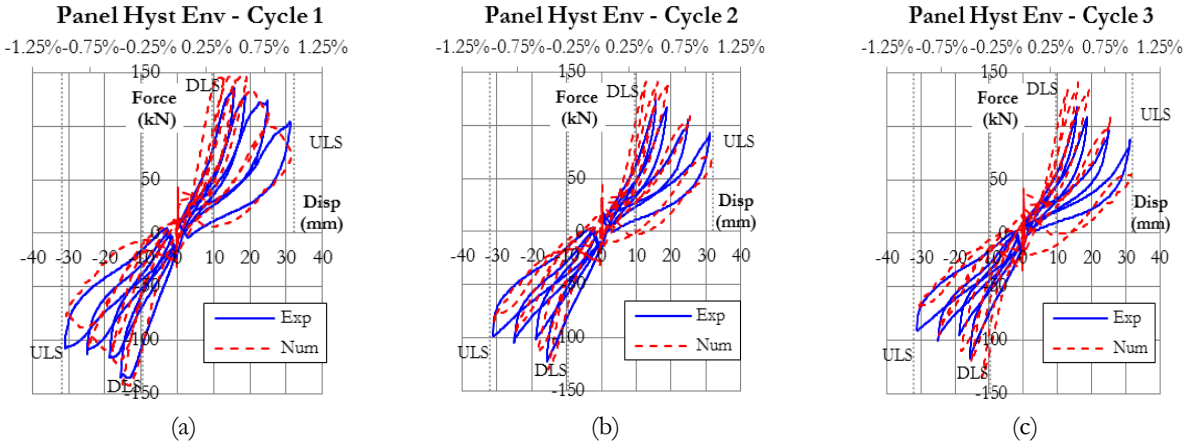

Figure 19: Effect of repeated cycles on the shape of the hysteresis for the open infill configuration.

3.3 Energy Dissipation

The normalized energy dissipation considers the accumulated displacement path during a half cycle. In contrast to viscous damping, hysteretic damping has a maximum effect at maximum deformation.

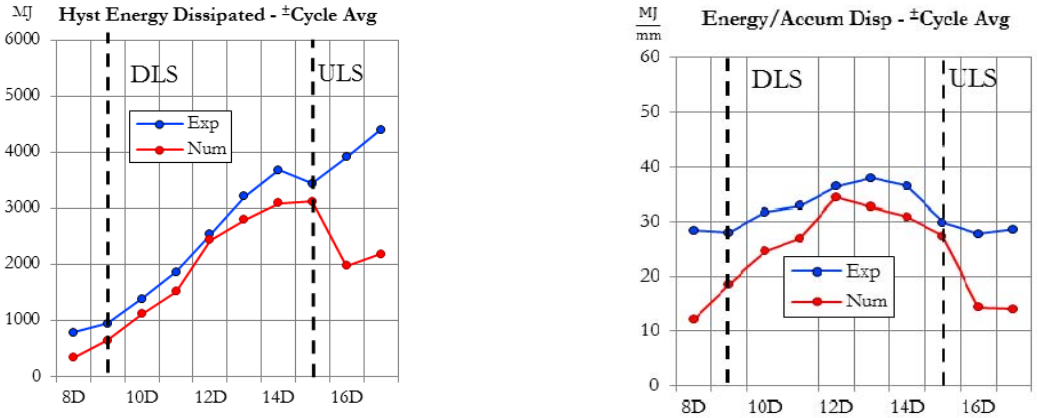

Figure 20: Total (left) and normalized (right) hysteretic energy model comparison, full infill.

The averaged energy dissipation for the full infill configuration shows a good match between the damage and ultimate limit state, although the numerical model consistently underestimates energy dissipation because the reloading branch cannot be adjusted. Consequentially, a compromise is found between the unloading stiffness and the energy dissipated per cycle.

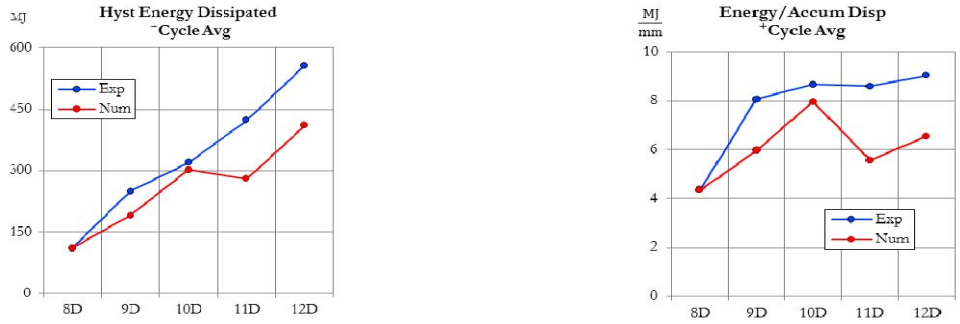

Figure 21: Total (left) and normalized (right) hysteretic energy model comparison, open infill.

Note the drop below the original normalized energy dissipation at the ultimate limit state in Figure 20. The visual damage and initiation of expulsions from the panel observed during testing correlate quantitatively the hysteretic properties of the infill's effect. The open infill hysteretic energy is constantly increasing with target drift for the experiment on the infilled frame with the opening. Unfortunately, the numerical model is unable to capture that behavior well, as a sudden drop occurs at target 11D in Figure 21.

3.4 Stiffness Reduction

The secant unloading stiffness is important and may be indirectly controlled by changing γ_{un}, which effects the sudden drop immediately at the onset of unloading. Figure 22 indicates that γ_{un} should increase with drift, as the numerical model is overestimating the unloading stiffness at smaller displacement cycles.

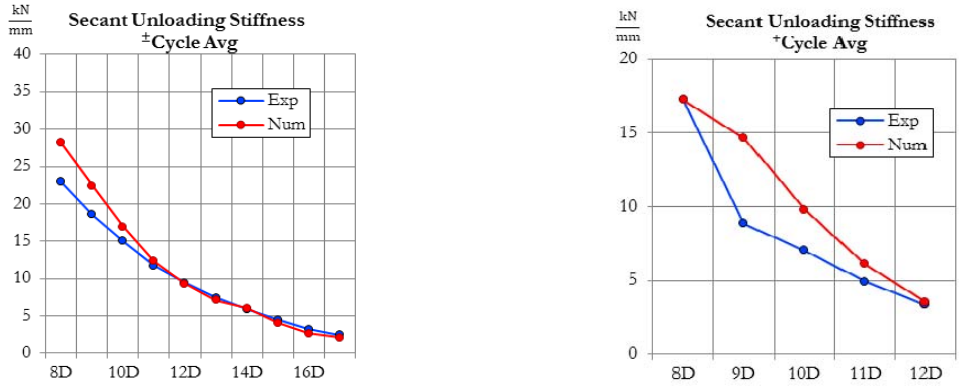

Figure 22: Secant unloading stiffness per cycle for the full and open infill configuration.

3.5 Overview

Figure 23 and 24 convey the sequence of the calibration procedure, from the bare frame model to the strut calibration and finally to the final combined infilled frame response.

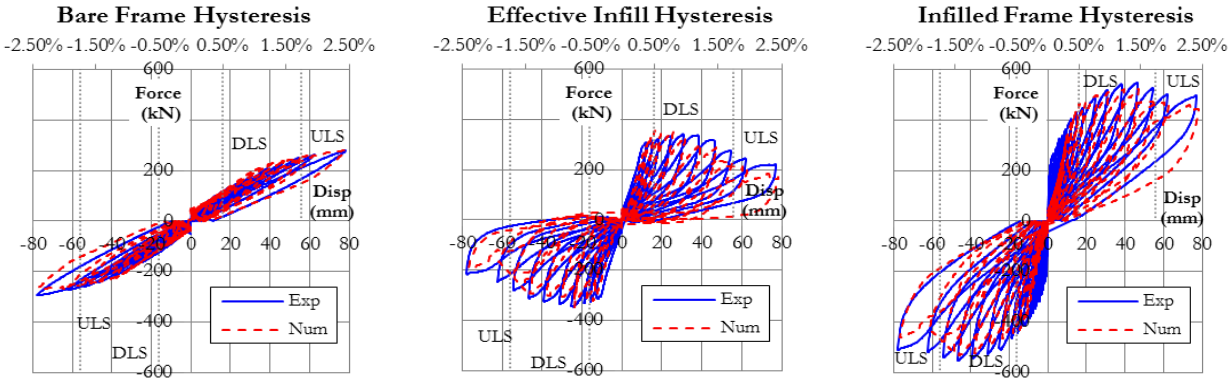

Figure 23: The bare frame, infilled frame and infill hysteresis for the full infill configuration.

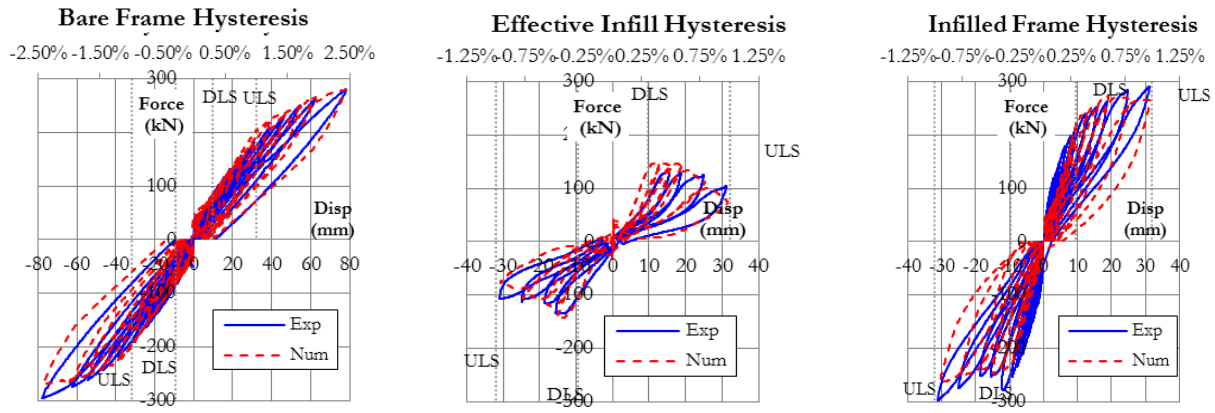

Figure 24: The bare frame, infilled frame, and infill hysteresis for the first cycles of the full and open infill configurations.

4 CONCLUSIONS

The calibration procedure presented focuses on accurately modeling the seismic performance of RC frame buildings infilled with a strong masonry typology. A series of cyclic tests on an RC frame subassembly with a full infill panel, an open infill panel and the infill panel omitted have taken place after a detailed characterization of the masonry. The cyclic testing of the bare and infilled frames at matching target drifts have allowed a unique interpretation of the data to which the single strut has been calibrated. The extracted hysteresis from the data represents the infill shear contribution in addition to changes in the RC frame response. The modeling of local effects has been circumvented by also considering the change in the frame response during the calibration of the strut. The strong masonry infill typology exhibits significant post-peak displacement capacity. The shape of the backbone curve of the uniaxial stress-strain constitutive model has two strength plateaus for the full infill panel.

The shape of the envelopes have been set prior to the optimization of hysteretic and strength parameters. The method uses a set of error criteria to help identify the best combination of parameters without particular bias. The generated error surfaces have been inverted to show the global maximum corresponding to the best accuracy. The final parameters show a good comparison to the full scale tests and can be applied to other frame geometries by extrapolating the parameters with adjustment to the empirical equations for consideration of the strong infill typology.

REFERENCES

[1] Morandi, P., Hak, S., and Magenes, G. (2014). In-plane experimental response of strong masonry infills. *International Masonry Conference.* Guimaraes: International Masonry Society.

[2] Hak, S., Morandi, P., Magenes, G., Sullivan, T. (2012). "Damage control for clay masonry infills in the design of RC frame structures," Journal of Earthquake Engineering, Vol. 16, S1, pp. 1-35.

[3] Maheri, M. R., Najafgholipour, M. Q., and Rajabi, R. (2011). The influece of mortar head joints on the in-plane and out-of-plane seismic strength of brick masonry walls. *Transactions of Civil and Environmental Engineering*, *35*, pp. 63-79.

[4] CEN (2004a). *Eurocode 8.* Brussels, Belgium: EN 1998-1, European Committee for Standardisation, ENV 1996-1-1.

[5] NTC08 (2008). *Norme tecniche per le costuzioni.* Rome, Italy: Ministero delle Infrastrutture.

[6] Giberson, M.F. (1967) "The response of nonlinear multi-story structures subjected to earthquake excitation," *EERL Report*, California Institute of Technology, Pasadena, California.

[7] Fukada, Y. (1969). Study on the restoring force characteristics of reinforced concrete buildings (in Japanese), Proceedings, Kanto District Symposium, Architectural Institute of Japan, Tokyo, Japan, No. 40.

[8] Stafford Smith, B. "Behavior of square infilled frames", ASCE Proceedings, February 1966, pg. 381-403.

[9] Dawe, J. L., and Seah, C. K. (1988). Lateral load resistance of masonry panels in flexible steel frames. *Proc. 8th International Brick and Block Masonry Conference.* Dublin, Ireland.

[10] Carr, A. J. (2007). *Ruamoko Manual.* University of Cantebury, Christchurch, New Zealand.

[11] Crisafulli, F. J. (1997). Seismic Behavior of Reinforced Concrete Structures with Masonry Infills. PhD Thesis. University of Cantebury, Christchurch, New Zealand.

[12] Sargin M., Ghosh S.K., Handa V.K. (1971) Effects of lateral reinforcement upon the strength and deformation properties of concrete. Mag Concr Res 23(75–76):99–110

[13] Holmes, M. (1961). Steel frames with brickwork and concrete filling. *Proceedings of the Institute of Civil Engineers*, pp. 473-478.